31st EUROPEAN ROTORCRAFT FORUM

Session Active Rotor Control
Paper #043

WEAK COUPLING FOR ACTIVE ADVANCED ROTORS

Analysis of a 2/rev Control Law for Power Reduction on a Trimmed Servo Flap Rotor using CFD

by

M. Dietz*, E. Krämer*, S. Wagner*, A. Altmikus**

*INSTITUT FÜR AERO- & GASDYNAMIK, UNVERSITÄT STUTTGART,
70550 Stuttgart, Germany
**EUROCOPTER DEUTSCHLAND GmbH, 81663 München, Germany

SEPTEMBER 13 - 15, 2005
FLORENCE
ITALY

WEAK COUPLING FOR ACTIVE ADVANCED ROTORS

M. Dietz*, E. Krämer*, S. Wagner* and A. Altmikus**

*Institut für Aerodynamik und Gasdynamik, Universität Stuttgart, Stuttgart, Germany
** Eurocopter Deutschland GmbH, Munich, Germany

Abstract

This paper presents a weak coupling method between a Navier-Stokes flow solver and a flight mechanics code. The method is applied to an active advanced rotor configuration in steady forward flight. Two scenarios are compared for one common forward flight case at a moderate advance ratio of 0.3. The first scenario features a trimmed rotor (passive) only, whilst the second uses an active trailing edge servo flap to introduce an additional 2/rev control (active rotor). Both calculations are trimmed for thrust, lateral and longitudinal mast moment. The principal interest of this investigation was the mean rotor power change due to the flap control law. A systematic increase of power consumption was observed for the active rotor, although a phase sweep of the control law revealed a minimum power phase angle. It can be concluded, that the weak coupling is well suited for systematic higher harmonic control law investigations. However an investigation of power reduction may be more interesting for greater advance ratios, where strong transonic effects and a pronounced dynamic stall influences the power consumption more severely.[1]

Nomenclature

Symbols

μ	advance ratio
Ma	Mach number
θ_0	collective pitch angle [°]
θ_{1c}	longitudinal cyclic pitch [°]
θ_{1s}	lateral cyclic pitch [°]
α_q	rotor shaft angle [°]
C_T	thrust coefficient
C_Q	torque coefficient
C_{Mx}	rotor mast roll moment coefficient
C_{My}	rotor mast pitch moment coefficient
C_nMa^2	sectional normal force coefficient
C_mMa^2	sectional pitching moment coef.
$C_{Fz}Ma^2$	sectional thrust coefficient (in z-direction of rotating system)
$C_{Fy}Ma^2$	sectional drag coefficient (in y-direction of rotating system)
$C_{Mx}Ma^2$	sectional moment coefficient (around x-direct. of rotating system)
N	Number of harmonic
Ψ	Azimuth angle
φ	Phase angle of the HHC-law

Coordinate Systems

Both the rotating rotor hub system and the non-rotating rotor hub system correspond to the definitions used by HOST.

Rotating rotor hub system:
- x-axis in radial direction from root to tip
- y-axis in tip path plane from trailing edge to leading edge
- z-axis in rotor hub direction

Non-rotating rotor hub system:
- x-axis longitudinal pointing backwards
- y-axis lateral pointing to starboard
- z-axis in rotor hub direction

According to the HOST convention an upward flap deflection is denoted as positive.

Trim numbering

- The initial HOST trim is denoted as 0^{th} trim.
- The FLOWer calculation following the n^{th} HOST trim is denoted as n^{th} FLOWer trim.

Acronyms

CFD	Computational Fluid Dynamics
CHANCE	Complete Helicopter Advanced Computational Environment
CSM	Computational Structure Mechanics
DLR	Deutsches Zentrum für Luft- und Raumfahrt e.V.
DOF	Degree Of Freedom
ECD	Eurocopter Deutschland GmbH
HOST	Helicopter Overall Simulation Tool
IAG	Institut für Aerodynamik und Gasdynamik
LARS	Lagerloses Aktives Rotor System
HHC	Higher Harmonic Control (Below the swash plate)
IBC	Individual Blade Control (Above the swash plate)

Introduction

In the case of helicopter rotors, a meaningful comparison of numerical simulations with

experimental data requires identical flight conditions. This is generally achieved by trimming the numerical aircraft, or rotor, by means of freed control inputs, towards a prescribed set of objectives. The control inputs are collective and cyclic pitch angles (θ_0, θ_{1c}, θ_{1s}). The selected trim objectives (which have been previously identified from flight test data) are the lift and the longitudinal and lateral mast moments (F_z, M_x, M_y) for an isolated rotor. This objective is achieved by iteratively adjusting the control values in order to meet the trim conditions of the experimental flight. In this study the rotor shaft angle α_q is fixed.

When different design characteristics of a rotor are studied with respect to performance benefits like noise and vibration reduction or performance gain the same principle must be applied i.e. maintaining identical trim objectives for each case. The phase angle of the control law for a flap of an active rotor is a potential design characteristic for such an investigation. Other characteristics may be the flap amplitude or different higher harmonics.

A particular difficulty in obtaining a conclusive prediction of benefits arises from the fact that the discrete flap sheds a highly complex, unsteady and three-dimensional vortex system from each extremity. These phenomena can not be captured by a blade element method. Therefore, a strong interest exists in using a vortex capturing approach. This is achieved in the form of a CFD solution in conjunction with a flight mechanics tool. To arrive at the necessary trimmed CFD solution, different methods have been developed. Apart from the relative resource consuming trim of a strong coupled, i.e. time accurate CFD-CSM simulation,[2] weak coupling, which relies on the exchange of harmonic boundary conditions is a well suited, cost efficient, alternative[3], [8]. For active flaps this method requires a grid deformation algorithm capable of deforming the trailing edge region in arbitrary chord-wise and radial extension.

Wind tunnel experiments on HHC and IBC strongly suggest that a performance gain of about 5% can be realised with a 2/rev control input.[4],[5] The numerical study of Cheng et al.[6] on a 2/rev IBC control substantiates this and thus the question arises if this is also possible for an active flap rotor. Patt et al. indicate that such a gain for an active flap would not be the case.[7] Since both these numerical studies lack a comprehensive non-linear description of the aerodynamic flow field around the rotor it seemed a natural progression to use the weak coupling to eliminate this shortcoming.

Numerical Methods

Structure model (HOST)

The EUROCOPTER flight mechanics tool HOST[9] represents a computational environment for simulation and stability analysis of the complete helicopter system. It enables the study of single helicopter components like isolated rotors as well as complete configurations with related substructures.

As a general purpose flight mechanics tool, HOST is capable of trimming the rotor based on a lifting-line method with 2D airfoil tables. For the flap, an additional interpolation is done in the polar curves depending on the flap angle.

Since the active rotor of Eurocopter Deutschland is conceived as a servo-flap rotor,[10] the elastic motion is also of great importance for a reliable prediction.

The elastic blade model in HOST considers the blade as a quasi one-dimensional Euler-Bernoulli beam. It allows for deflections in flap and lag direction and elastic torsion along the blade axis. In addition to the assumption of a linear material law, tension elongation and shear deformation are neglected. However, possible offsets between the local cross-sectional centre of gravity, tension centre and shear centre are accounted for, thus coupling bending and torsional DOFs.

The blade model is based on a geometrically non-linear formulation, connecting rigid segments through virtual joints.[11] At each joint, elastic rotations are permitted about the lag, flap and torsion axes. Since the use of these rotations as degrees of freedom (DOFs) would yield a rather large system of equations, the number of equations is reduced by a modal Rayleigh-Ritz approach. A limited set of mode-like deformation shapes together with their weighting factors are used to yield a deformation description. Therefore, any degree of freedom can be expressed as,

$$h(r,\psi) = \sum_{i=1}^{n} q_i(\psi) \cdot \hat{h}_i(r) \qquad (1)$$

where n is the number of modes, q_i the generalized coordinate of mode i (a function of the azimuth angle ψ), and $\hat{h}_i$ is the modal shape (a function of the radial position r).

Aerodynamic model (FLOWer)

In the present study FLOWer[12] has been used for the aerodynamics, which is available at IAG and ECD through the cooperation with the DLR (Deutsches Zentrum für Luft- und Raumfahrt e.V.) in the framework of the CHANCEII project. FLOWer solves the three-dimensional,

unsteady Euler or Reynolds-averaged Navier-Stokes equations in order to analyze the flow field around the helicopter rotor. These equations are formulated in a hub attached, non-inertial, rotating frame of reference, with explicit contributions of centrifugal and Coriolis forces. See [13] for details of the algorithm.
The discretisation of space and time is separated by the method of lines using a cell-vertex or cell-centered finite volume formulation. Spurious oscillations of the central difference scheme are suppressed by first and second order artificial dissipation. The time integration makes use of the dual time stepping technique with a second order implicit time integration operator.[14]
FLOWer features the Chimera-technique,[15] allowing for arbitrary relative motion of aerodynamic bodies. Body fitted grids around each blade are embedded in a background grid (Figure 1), in which the blade vortex sheets are convected from one blade grid to the next. The elastic deformation of the blade can be introduced into the body fixed mono-block grids by an algebraic deformation method for OH- and CH-topologies.[16]

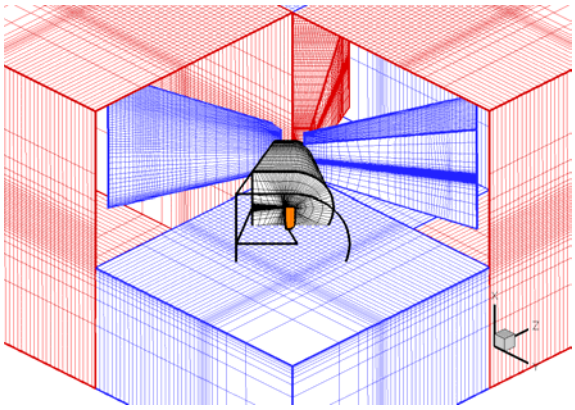

Figure 1: Chimera grid set-up

Algorithmic Developments

Weak Coupling

The iterative coupling scheme used for the present work basically corresponds to the technique used in [3] and [2]. HOST uses CFD loads to correct its internal 2D aerodynamics and re-trims the rotor. The blade dynamic response is introduced into the CFD calculation in order to obtain updated aerodynamic loads. This cycle is repeated until the CFD loads match with the blade dynamic response evoked by them. A criterion for this converged state is given by the change in the free controls with respect to the preceding cycle. Convergence has been reached after the changes in the controls have fallen below this imposed limit. All calculations of this paper have been trimmed until the change in the free controls θ_0, θ_{1c}, θ_{1s} is less than 0.005°.
The specific steps of the coupling procedure are thus given as follows:

1. HOST determines an initial trim of the rotor based on its internal 2D aerodynamics derived from airfoil tables. The complete blade dynamic response for a given azimuth angle is fully described by the modal base and the related generalized coordinates.
2. The blade dynamic response is taken into account in the succeeding CFD calculation by the reconstruction of the azimuth angle dependent blade deformation from the modal base and the respective grid deformation of the blade grid.
3. The CFD calculation determines the 3D blade loads in the rotating rotor hub system (F_x[N/m], F_y[N/m], F_z[N/m], M_x[Nm/m], M_y[Nm/m], M_z[Nm/m]) for every azimuth angle and radial section of the blade.
4. For the next trim HOST uses a load given by,
$$\overline{F}^{n}_{HOST} = \overline{F}^{n}_{2D} + \overline{F}^{n-1}_{3D} - \overline{F}^{n-1}_{2D} \qquad (2)$$
$\overline{F}^{n}_{2D}$ represents the free parameter for the actual HOST trim. A new dynamic blade response is obtained which is expressed by an update of the generalized coordinates.
5. Steps (2) to (4) are repeated until convergence has been reached, i.e. when the difference
$$\Delta\overline{F}^{n} = \overline{F}^{n}_{2D} - \overline{F}^{n-1}_{2D} \rightarrow 0 \qquad (3)$$
tends to zero and the trim-loads depend only on the 3D CFD aerodynamics.

It is mandatory that the updated CFD loads for each successive trim are periodic with respect to the azimuth angle. After the CFD calculation has been restarted from the previous run, a certain number of time steps (i.e. a certain azimuth angle range) is necessary until the perturbation introduced by the updated set of generalized coordinates has been damped down and a periodic answer is obtained again. In fact, it is not necessary to continue the calculation until one fully periodic 1/rev response of an individual blade is obtained, as this can be composed from the last quarter revolution of all four rotor blades. It is therefore sufficient to run the CFD calculation until a periodic 4/rev behaviour of the complete rotor can be observed. Clearly, this state is reached

more quickly, the smaller the initial disturbance. For this reason the azimuth angle range covered by the CFD calculation can be reduced with an increasing number of re-trims. The changes in the free controls and the blade dynamic response become smaller from one re-trim to the next.
This weak coupling strategy was applied to the passive and active rotors in the same manner. In the case of the active rotor, HOST uses modified polar curves in the flap region for its internal 2D aerodynamics. From the CFD perspective the blade loading is directly influenced by the local grid deformation in the flap region. The resulting load distribution is taken into account by HOST for the rotor trim in the same way as for the passive rotor. Four re-trims were needed in order to achieve the required accuracy for the passive and active rotor.

Grid Deformation

In order to correctly model the dynamic behaviour of the rotor blade in the CFD solver, the blade must be deformed according to the output of the preceding HOST calculation. This requires the reconstruction of the blade elastic axis and its elastic twist for a given azimuth angle. The same strategy as used in HOST was adopted to describe the blade deformation. In HOST the blade is modelled as a chain of rigid elements which are connected to each other by fictive articulations. The blade deformation is therefore defined by the rotation angles about these articulations. The following steps have to be performed in FLOWer at the beginning of a physical time step in order to reconstruct the blade deformation:

1. Sum up the generalized coordinates over all harmonics for all modes, taking into account the current azimuth angle of the blade.
2. Amplify every mode with the respective generalized coordinate.
3. For every articulation sum up the contributions of all modes to give the respective rotation angle.
4. Locally add the precone, prelag and pitch angle to the respective rotation angle.
5. Starting at the rotor hub, generate the deformation of the elastic axis by concatenating all rotations, element by element.
6. Apply elastic torsion element by element.
7. Perform interpolation on the spanwise discretisation of the CFD grid.

As it can be seen from this description, all flap and lag rotations (including precone and prelag) and the blade pitch are part of the kinematic chain, whereas elastic torsion is not and is applied afterwards. Figure 2 shows a comparison of flap deflection and elastic torsion between HOST and FLOWer for the passive rotor in trimmed state at $\psi = 90°$. Here, both the elastic axis and elastic torsion match very well.

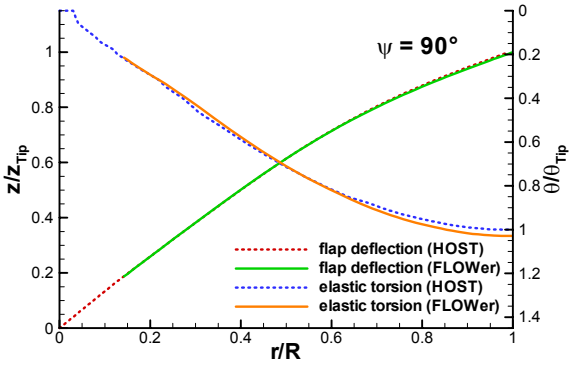

Figure 2: Comparison of elastic axis (including pre-cone at r/R=0) and elastic torsion between FLOWer and HOST

In order to minimize the deformation which must be treated by the grid deformation algorithm, the description of the elastic axis and the blade torsion is transferred from the rotating rotor hub system to the blade secantial coordinate system which is aligned from the blade root towards the blade tip. Thus the update of the blade grid can be decomposed into two parts: A rigid body rotation of the complete grid into the secantial system and a grid deformation relative to this system.

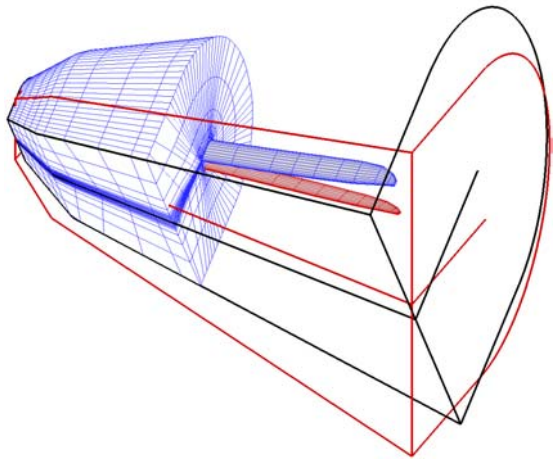

Figure 3: Blade grid deformation

This process is illustrated by Figure 3, which shows the undeformed blade surface and block boundary (red) together with the deformed surface and a section of the deformed grid (blue). The grid deformation algorithm is based on Hermite polynomials and keeps the outer block boundaries constant.
In the case of the active rotor, the flap deflection is introduced as a local grid

deformation of the blade surface in the flap region. As the flap is modelled as a pure grid deformation the slit at the inner and outer flap boundary cannot be reproduced. However, all relevant consequences of a flap deflection (e.g. influence on blade surface pressure distribution, jump in circulation, vortex shedding etc.) are correctly modelled, thus this flaw in the modelling is acceptable. At the flap boundaries the flap deflection is reduced to zero within a certain smoothing range. For the present investigation the extent of this smoothing area was minimized due to a radial clustering of the blade grid in the relevant regions. The flap model which has been introduced into FLOWer is able to model several flap segments which can be individually deflected using a (higher) harmonic control law. In the case of the active rotor the deformation process due to weak coupling acts upon a pre-deformed blade surface which contains the deflections of the flap segments.

Test Case Description

For the present investigation a forward flight case with a medium advance ratio of $\mu = 0.3$ was selected. For both the passive and the active rotor the shaft angle was held fixed at α_q*=-4.9°* and the calculations were trimmed for thrust, lateral and longitudinal mast moment by adaptation of the free controls θ_0, θ_{1c}, θ_{1s}. Flight condition and trim objective are summarized in Table 1.

The active ATR-A rotor blade features three adjoining flap segments with a chordwise extent of 15% chord and the radial positions *r/R = 0.69 – 0.75*, *r/R = 0.75 – 0.8* and *r/R = 0.8 – 0.85*. For the present calculations a common control law was used for the innermost and the central flap segment, whereas the outermost segment remains fixed at zero deflection. The 2/rev flap control law is given by:

$$A(t) = A_0 \cdot \cos(2 \cdot \Omega \cdot t - 2 \cdot \varphi) \qquad (4)$$

The flap amplitude was prescribed to $A_0 = 6°$. With an increment in azimuth of $\Delta\varphi = 30°$ for the rotor, a $\Delta\varphi' = 60°$ resolution of the phase shift in the control law has been investigated.

Table 1: Flight condition and trim objective

Flight speed Mach number	0.21
Blade tip Mach number	0.64
Blade tip Reynolds number	4.7×10^6
Rotor shaft angle	-4.9 deg
Far field pressure	84400 Pa
Far field temperature	279 K
Thrust coefficient	0.008
Rotor mast pitch moment cf.	-0.636×10^{-4}
Rotor mast roll moment coef.	-0.193×10^{-4}

The CFD computations have been carried out using a Chimera grid system which is depicted in Figure 1. The Chimera grid setup consists of four monoblock blade grids with C-topology and a cartesian 4-block background grid. The grid resolutions are given in Table 2. The blade grid used for the active rotor calculations features a slightly higher number of cells than the passive rotor grid due to the additional radial clustering at the flap segment boundaries.

Table 2: Grid resolution

Grid	**Resolution**	**Number of cells**
Blade grid (passive)	169x41x61	403,200
Blade grid (active)	185x37x85	556,416
Background grid	4 x 65x73x73	4 x 331,776

The Baldwin&Lomax turbulence model with Degani-Schiff modification was chosen for the closure of the RANS equations and an azimuthal resolution of 1° per timestep was used.

All computations were carried out on the NEC SX8 supercomputer of the High Performance Computing Center of Stuttgart. The 8-block grid setup allowed for a parallel FLOWer run on eight CPUs (one SX8 node) with reasonable load balancing. The computation reached an overall performance of 21 GFLOPs and the calculation of one revolution took approximately seven hours wall clock time.

Results

In the following sections “Passive Rotor” and “Active Rotor” the discussion will focus on the performance of the trim procedure and the qualitative flow field. A detailed look on the differences between the active and the passive rotor, especially with respect to rotor performance, will be given in sections “Active Control” and “Passive versus Active Rotor”.

Passive Rotor

In Figure 4 the unsteady aerodynamic rotor loads are shown for the complete weak coupling process. Each re-trim is marked off with respect to the preceding trim by the line type change from solid to dash. It can be clearly seen that the disturbance introduced by the update of the blade dynamic response

decreases from each retrim cycle to the next as the procedure converges towards the trimmed state. After four retrims (seven rotor revolutions) the calculation has reached the trimmed state with the required accuracy and the thrust coefficient has reached the trim objective of C_T = *0.008*. The corresponding development of the free controls is given later in Figure 16 to Figure 18.

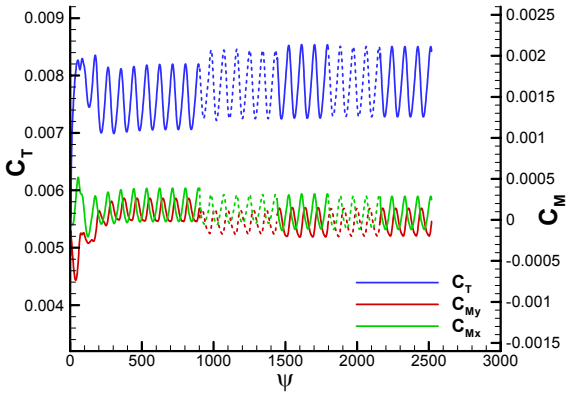

Figure 4: Unsteady rotor coefficients during the coupling process (passive rotor)

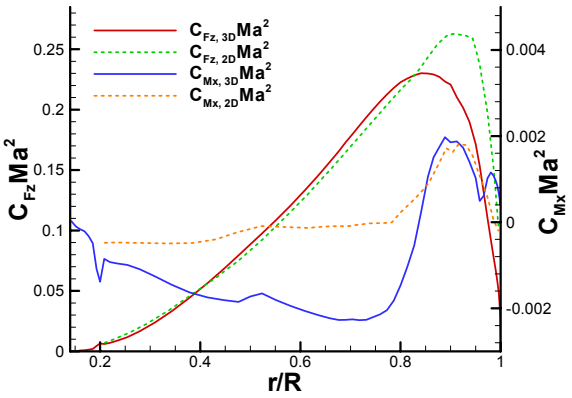

Figure 5: Comparison between HOST loads and CFD loads at ψ=*0°* (passive rotor)

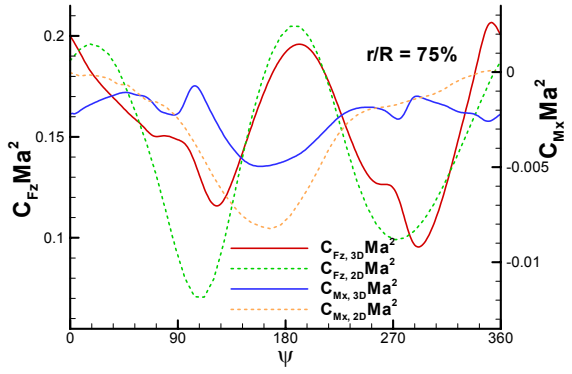

Figure 6: Comparison between HOST loads and CFD loads at *r/R=0.75* (passive rotor)

Figure 5 and Figure 6 show comparisons between the 2D HOST loads and the CFD loads, both given in trimmed state (re-trim 4). Figure 5 shows the radial distribution of thrust and pitching moment at ψ*=0°*, whereas the azimuthal distribution at *r/R=0.75* is compared in Figure 6.

Although HOST correctly predicts the overall characteristics of the load distributions, differences between 2D and 3D aerodynamics can be observed in both figures. In Figure 5 HOST predicts a pitching moment of around zero within a wide radius range, whereas the CFD pitching moment is slightly negative. On the other hand the positive peak in the $C_{Mx}Ma^2$-distribution near the blade tip is predicted correctly. Looking at the azimuthal comparison of Figure 6 the most significant differences arise at the advancing blade side and at the retreating blade side. The additional oscillations visible both in the $C_{Fz}Ma^2$-distribution and the $C_{Mx}Ma^2$-distribution are not reproduced by HOST.

The pressure distribution on the blade surface is depicted in Figure 7 for the four azimuth angles ψ*=0°*, ψ*=90°*, ψ*=180°* and ψ*=270°*. The C_p-distributions at *r/R=0.75* for the same azimuth positions are given in Figure 8. The typical features of a rotor flying at a moderate advance ratio can be summarized as; an extensive low pressure region in the outer radial region on the advancing blade side (but no shock), an area of reversed or separated flow in the inner radial region on the retreating blade side and more or less similar flow conditions at ψ*=0°* and ψ*=180°*.

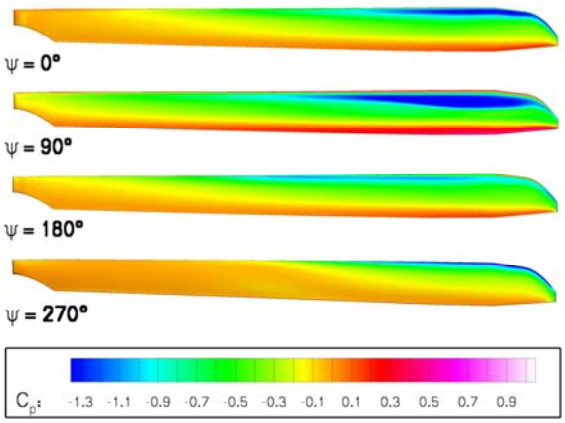

Figure 7: Surface pressure distribution of passive rotor

The qualitative flow field is shown in Figure 9. The vortex system generated by the rotor is visualized with the well known λ_2-criterion of Jeong and Hussain[17]. An iso-surface of λ_2 = *-0.0001* has been chosen for visualization. Both

the blade tip vortex system and the inboard wake are visible. Naturally no blade vortex interaction is observed at this flight condition.

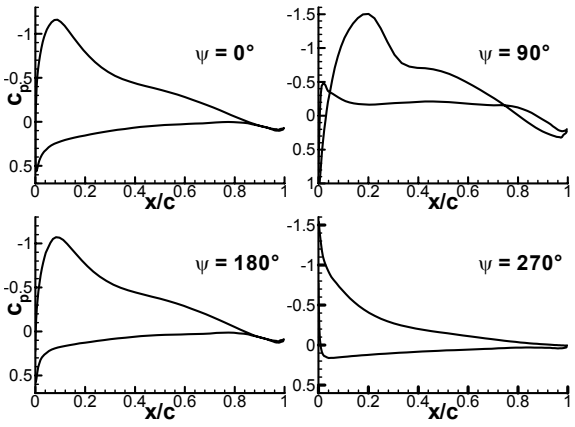

Figure 8: C_p-distributions at r/R=0.75 for passive rotor

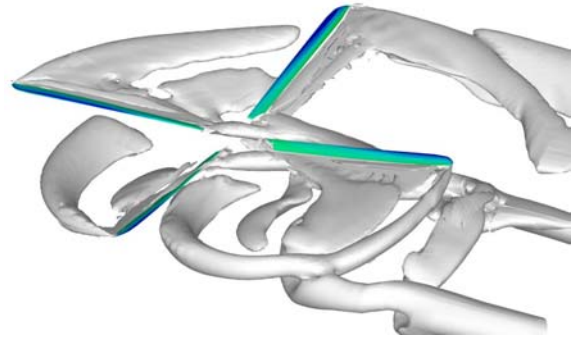

Figure 9: Vortex system of passive rotor (λ_2 = *-0.0001)*

Active Rotor

In this section we present exemplarily the results for the flap phase angle φ =*0*°, this means the flap reaches its maximum upward deflection at ψ =*0*° and ψ =*180*°.

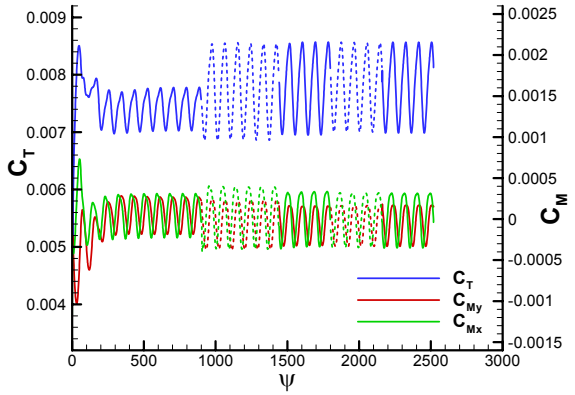

Figure 10: Unsteady rotor coefficients during the coupling process (active rotor, φ =*0*°)

Figure 10 shows the unsteady aerodynamic rotor loads versus azimuth angle for the coupling process. It can be stated that the trim procedure works for the active rotor with the same quality as for the passive. Four retrims are necessary in order to obtain a trimmed state. A comparison of the development of the free controls for all flap phase angles will be made in the following section.

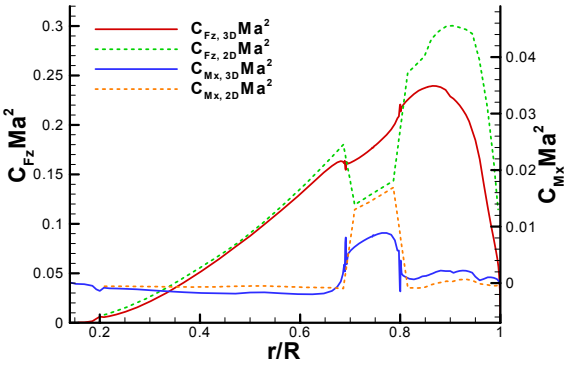

Figure 11: Comparison between HOST loads and CFD loads at ψ=*0*° (active rotor, φ = *0*°)

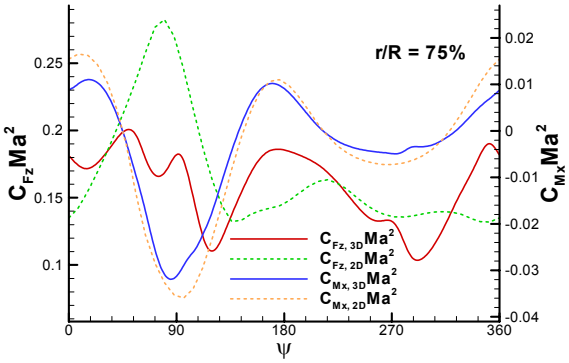

Figure 12: Comparison between HOST loads and CFD loads at *r/R=0.75* (active rotor,φ = *0*°)

The influence of the flap control on the aerodynamic loads can be seen in Figure 11 and Figure 12. As presented above for the passive rotor, these figures compare the 2D HOST loads with the CFD loads in trimmed state. From Figure 11 it can be seen that the flap influence predicted by the CFD solution does not show as strong discontinuities as are obtained by HOST. This smoothing, which is especially pronounced for the thrust distribution, is caused by the counter-rotating vortices shed from the flap boundaries. The induced velocities caused by these vortices produce a radial smoothing of the effective angle of attack and thus a smoothing of the thrust. Clearly, such three-dimensional flow effects cannot be captured by the HOST aerodynamic model.

The radial position shown in Figure 12 is located around the centre of the flap range. It can be stated that the agreement in the pitching moment between the 2D HOST aerodynamics and CFD is good throughout the complete azimuth range (but note the difference in the $C_{Mx}Ma^2$-scaling compared to Figure 6). The $C_{Mx}Ma^2$-distribution is clearly dominated by the 2/rev flap control input, leading to a pitch-up moment at $\psi = 0°$ and $\psi = 180°$ (upward flap deflection) and a nose-down moment at $\psi = 90°$ and $\psi = 270°$ (downward flap deflection). In contrast to the good agreement in $C_{Mx}Ma^2$, the agreement in the thrust distribution $C_{Fz}Ma^2$ is poor. Three-dimensional flow effects lead to a greater concentration in higher harmonic oscillations on the advancing blade, which HOST is not able to predict.

Figure 13 and Figure 14 show the surface pressure and C_p-distribution, respectively at *r/R=0.75*. In Figure 13 the influence of the flap deflection is evident in the distortion of the pressure contours, which can be seen best for the advancing blade or for the C_p-distributions of Figure 14.

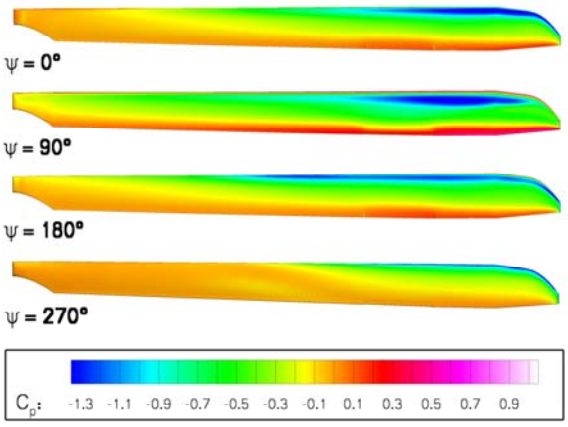

Figure 13: Surface pressure distribution of active rotor ($\varphi = 0°$)

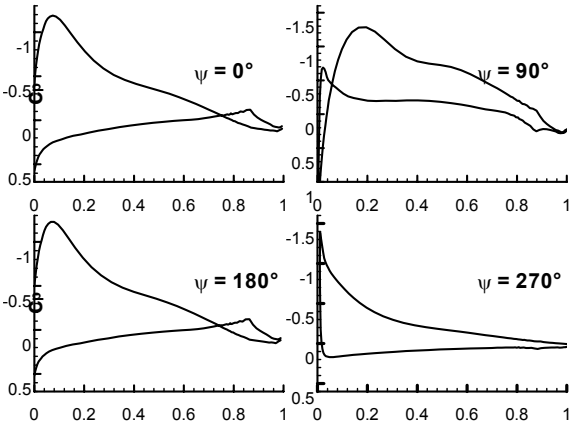

Figure 14: C_p-distributions at r/R=0.75 for active rotor ($\varphi = 0°$)

Significant differences between the active and the passive rotor can be observed with respect to the three-dimensional flow field. As expected, additional vortices are shed from the blade at the inner and outer flap boundaries. The strength of these vortices must not be underestimated, as seen from Figure 15. The interaction of the flap vortices with the blade tip vortex system and the inboard wake leads to a highly complex flow field which is difficult to predict.

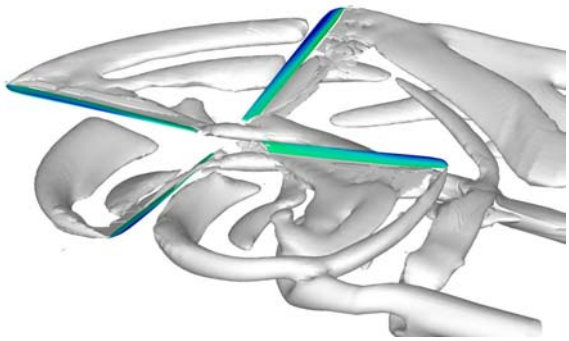

Figure 15: Vortex system of active rotor ($\varphi = 120°$, $\lambda_2 = -0.0001$)

Active Control

One of the main aspects of this paper is the investigation of a 2/rev flap control law with respect to the rotor performance, i.e. the required rotor power. For this purpose the rotor performance variation has been investigated for six different flap phase angles covering one period of the flap movement with a $\Delta\varphi' = 60°$ resolution.

The trim convergence of the control angles θ_0, θ_{1c} and θ_{1s} for all flap phase angles compared to the passive rotor is given in Figure 16 to Figure 18. For all computations all free controls converged to the required accuracy within four re-trim cycles. Even though a systematic deviation of the 0th HOST trim to the final trimmed state can be observed for all three controls, HOST is able to predict the influence of the variation of the flap phase on the rotor trim. All initial HOST computations require a larger (more negative) θ_{1s} input to achieve the required longitudinal mast moment and a slightly higher collective pitch.

The influence of the 2/rev flap control on the rotor performance is depicted in Figure 19 and Figure 20. The polar diagram of Figure 19 shows the relative power consumption of the active rotor with respect to the passive rotor. Both the performance predicted by HOST at its initial trim and the performance after the weak coupling procedure are plotted. The power consumption of the passive rotor at the 0th trim

has been chosen as the reference power. The relative power consumption is plotted on the radial axis, whilst the azimuthal increment of the flap phase is given on the circumferential axis.

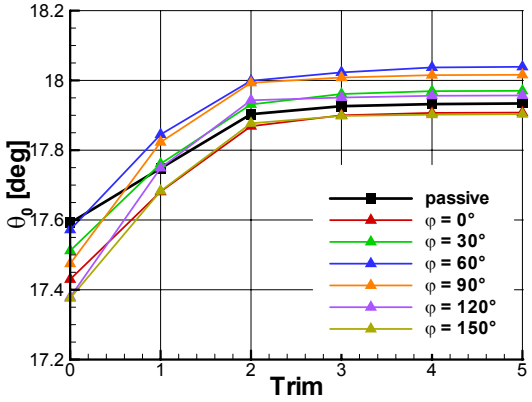

Figure 16: Convergence of collective pitch

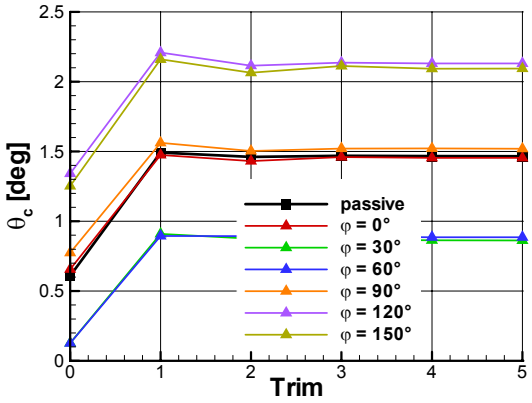

Figure 17: Convergence of longitudinal cyclic pitch

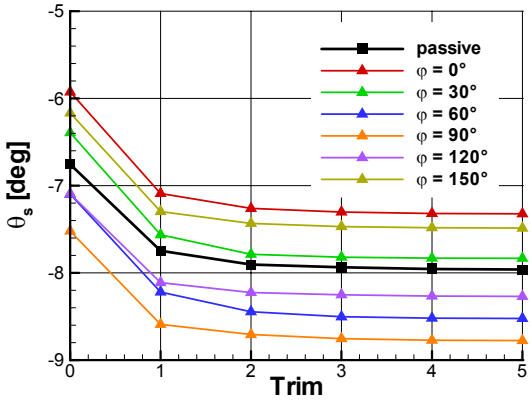

Figure 18: Convergence of lateral cyclic pitch

Using this plot style we obtain an elliptical shape for the required power, due to the fact that the flap control law is 2/rev and the plot is point-wise symmetrical. Looking at the phase variation predicted by the initial HOST trim, the active rotor requires approximately the same power as the passive one between $\varphi = 90°$ and $\varphi = 120°$. Outside of this region a higher power consumption can be observed for the active rotor. At $\varphi = 110°$ one might even expect a decreased power requirement. This is shown in detail by the trim 0 curve in Figure 20.

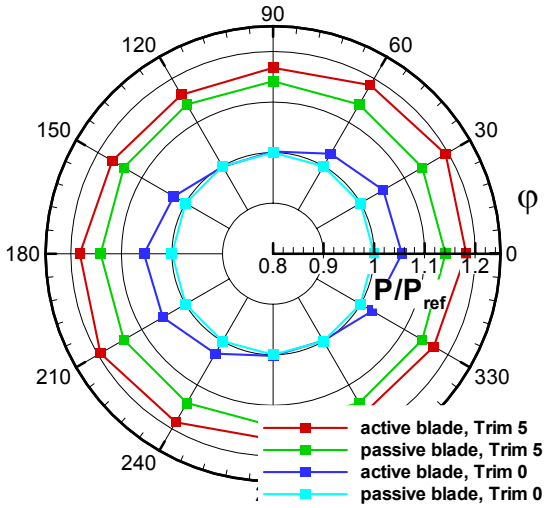

Figure 19: Rotor power over phase angle of control law

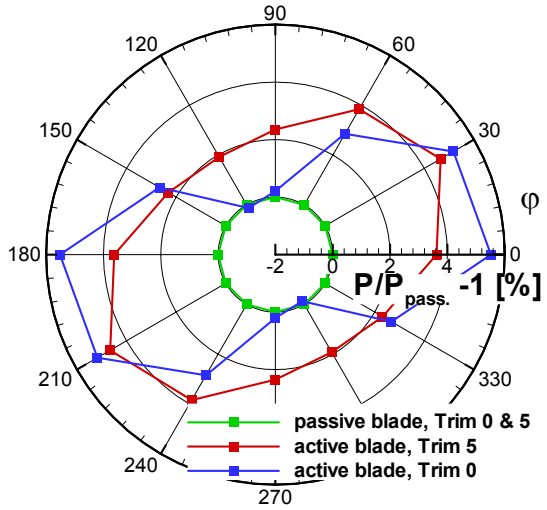

Figure 20: Rotor power over phase angle with respect to the passive rotor

The trimmed solution (trim 5), i.e. with 3D loads, generally predicts a higher power requirement compared to that for the initial trim (trim 0). A 14% increase is observed for the passive rotor. The active rotor performance diagram still maintains its elliptical shape, although the power requirement now entirely exceeds that of the passive rotor. Further, the phase angle for minimum power has slightly increased to about $\varphi = 120°$.

The power of the active rotor relative to the passive one, for both the initial and final trim, is given in Figure 20. As previously mentioned, the initial HOST trim predicts roughly 0% power increase for the active rotor compared to the passive one, at the optimum phase angle. The trimmed solution (with 3D loads) predicts an increase of 2% for the optimum phase angle.
This increase in power consumption is equivalent to an increase in rotor torque. Figure 21 shows the unsteady aerodynamic torque coefficient around the rotor axis in trimmed state. In agreement to the increase in power the mean torque, for the active rotor increases accordingly (larger negative values of C_Q).

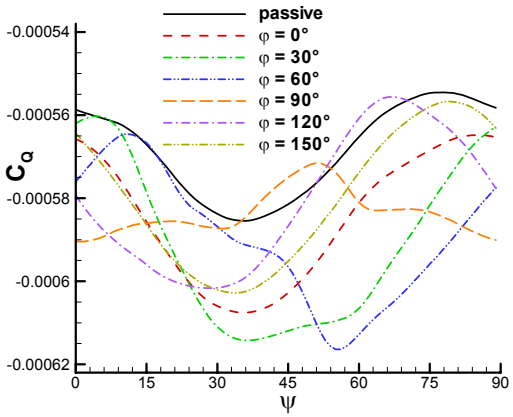

Figure 21: Unsteady aerodynamic torque in trimmed state

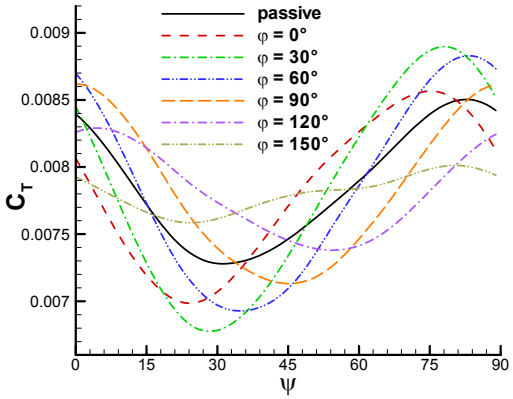

Figure 22: Unsteady aerodynamic thrust in trimmed state

Further, the flap input also affects the unsteady aerodynamic thrust, shown in Figure 22. Although the mean thrust is equal for all phase angles (the calculations were trimmed for thrust), the amplitude of the unsteady rotor thrust may be different. A flap control input with a phase angle of $\varphi = 150°$ results in a significant reduction of the amplitude of the aerodynamic thrust.

The main cause for the thrust variation is the servo flap effect. The flap is deflected and introduces an additional torsional moment about the feathering axis. This change in torsion is the principle reason for the thrust change. Figure 23 clearly shows that the 2/rev (tip) torsion is most sensitive to a 2/rev flap input, followed by the 3/rev and 1/rev. Higher harmonics are negligible. Reducing the torsional blade stiffness would even increase this effect and eventually, lower flap amplitudes might be needed to obtain the desired effect.

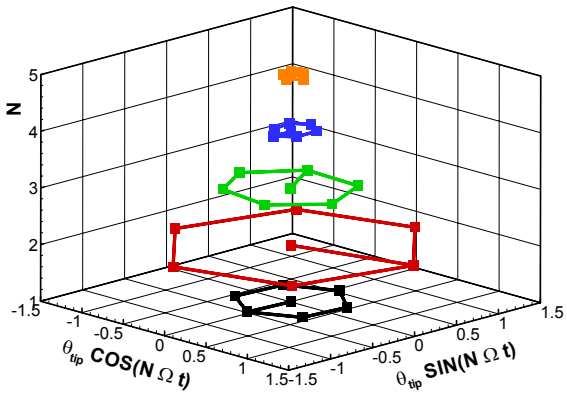

Figure 23: Torsion sensitivity; harmonic contributions to the tip torsion deflection depending on the phase of the flap control law; the centre points denote the passive rotor

The initial goal of the 2/rev control law investigated in the present work was the power reduction of the rotor. However, this was not observed for the investigated combination of control law and flight condition. It is assumed that the benefit of the additional 2/rev control is insufficient compared to the additional pressure drag caused by the flap deflection. However, it is expected, that a reduction of the flap amplitude might eventually lead to a power reduction for higher advance ratios greater than $\mu = 0.4$, where strong transonic effects and a pronounced dynamic stall influences the power consumption more severely.

Passive versus Active Rotor

As highlighted in the previous section the flap input with $\varphi = 120°$ phase angle resulted in the minimum power consumption. In this section, therefore the comparison of the passive and the active rotor will be restricted to this phase angle.
Figure 24 and Figure 25 show a comparison between the active and passive rotor for the coefficients C_nMa^2 and C_mMa^2. The radial position $r/R = 0.5$ (Figure 24) is inboard from the flap region and thus not directly affected by the flap deflection. However, the radial position

r/R=0.75 of Figure 25 is located within the flap range. For both radial positions minor differences in C_nMa^2 occur within the second half of the revolution. More significant differences are observed on the advancing blade side. The downward deflection of the flap at ψ *=30°* causes a nose-down twist of the blade. At *r/R=0.5,* C_nMa^2 is reduced compared to the passive rotor due to this negative twist. At *r/R=0.75,* the effective increase of the airfoil camber due to the flap deflection (and thus the increase of the effective angle of attack) must be taken into account, leading to an increase of C_nMa^2 despite of the nose-down twist. At ψ *=120°,* the opposite is true. The upward deflection of the flap leads to a nose-up elastic twist, which increases C_nMa^2 at *r/R=0.5*. At *r/R=0.75* the airfoil's effective angle of attack is reduced by the flap deflection, resulting in a lower value of C_nMa^2. Note the large influence of the flap deflection on the pitching moment, especially on the advancing blade side.

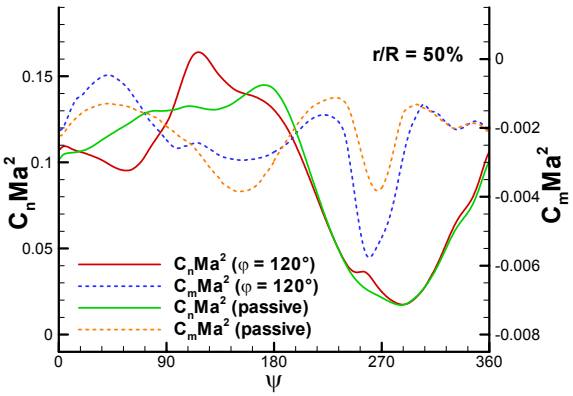

Figure 24: Comparison of C_nMa^2 and C_mMa^2 between active and passive rotor at r/R=0.5

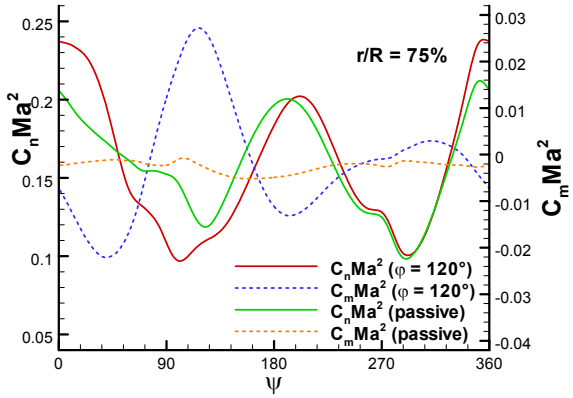

Figure 25: Comparison of C_nMa^2 and C_mMa^2 between active and passive rotor at r/R=0.75

These same effects but in an alternative representation can be observed in Figure 26 to Figure 28.

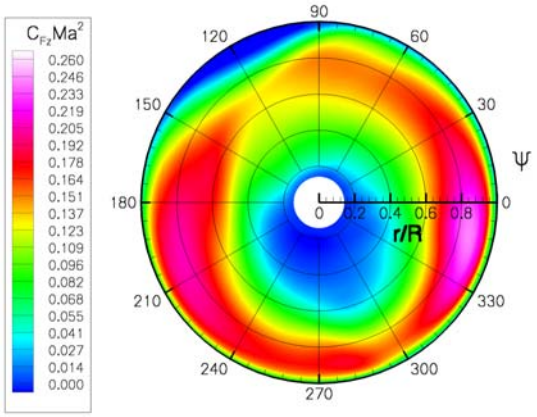

Figure 26: Thrust distribution over rotor disk for passive rotor

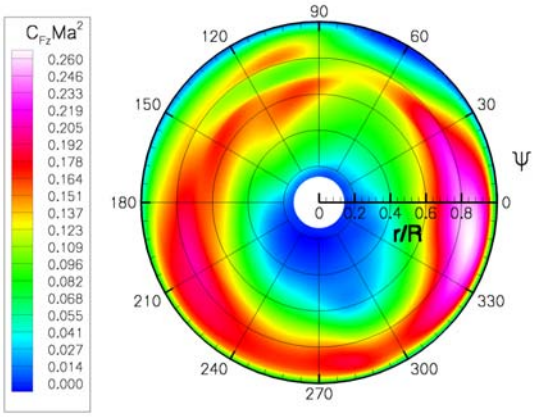

Figure 27: Thrust distribution over rotor disk for active rotor

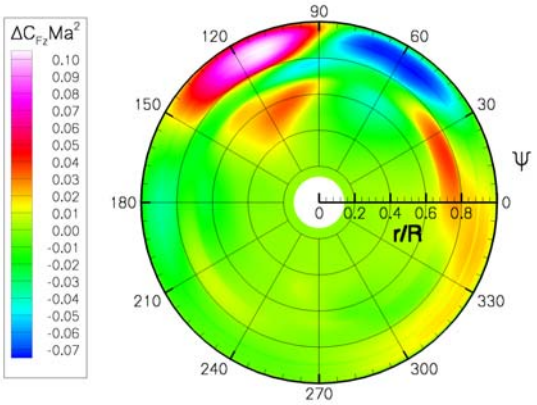

Figure 28: Difference in thrust distribution between active and passive rotor

Figure 26 shows the thrust distribution ($C_{Fz}Ma^2$) on the rotor disk for the passive rotor, Figure 27, the thrust distribution on the disk for the active rotor and Figure 28, the thrust difference between active and passive rotor. All figures use identical contour levels. As previously stated, only minor changes arise at the

retreating blade side. The advancing blade side of the passive rotor features an area which produces comparatively low lift, located around ψ *=120°*. However, for the active rotor (Figure 27) the upward deflection of the active flap and the consecutive nose-up twist of the blade results in an increase in lift over this area. In addition, the downward flap deflection at ψ *=30°* leads to a nose-down twist which reduces the lift in the range from ψ *=30°* to ψ *=90°*.

Therefore, it can be concluded, that (maintaining the same rotor trim) the active control leads to a redistribution of rotor thrust from the first to the second quadrant and thus, to a more equally distributed thrust on the first half of the rotor revolution.

The drag distribution ($C_{Fy}Ma^2$) on the rotor disk is given in Figure 29 to Figure 31. Note that F_y denotes the force in positive y-direction of the rotating rotor hub system according to the HOST convention. Therefore, a negative value signifies drag and a positive value a propulsive force in the rotor plane. In Figure 31 the difference in $C_{Fy}Ma^2$ between the active and the passive rotor is plotted. Thus, a negative value denotes higher drag of the active rotor compared to the passive one. Changes in the drag distribution can be observed on the whole rotor disk. The flap range of the active rotor can be identified as a ring-shaped area which is separated from the inner and outer radial region by discontinuous radial changes in $\Delta C_{Fy}Ma^2$. This can be explained by the fact that an upward deflection of the flap (ψ *=120°* and ψ *=300°*) results in a reduction of the effective airfoil camber and thus, a drag reduction (red areas). Whereas a downward deflection (ψ *=30°* and ψ *=210°*) increases the camber and therefore the drag (green areas). Over the rotor disk, areas of increased and reduced drag can be found. The influence on the mean value is thus hard to determine. But as seen from the previous section, the mean drag must have slightly increased, as the mean rotor torque has increased by 2%.

Finally, Figure 32 and Figure 33 show a comparison of active and passive rotor with respect to the blade dynamics. The blade tip flap deflection is given in Figure 32. Figure 33 shows the elastic tip torsion, for which a positive (nose-up) tip torsion corresponds to the positive axis direction of the θ/θ_{max}-axis. In addition to the trimmed solution (solid lines), the figures also contain the distributions of the initial HOST trim (dashed lines). The non-dimensional values shown in the figures have been obtained by norming with the maximum amplitude of the 0th HOST trim of the passive rotor.

Only minor changes can be observed for the tip flap deflection, both with respect to the difference between the initial HOST trim and the trimmed solution and with respect to the difference between active and passive rotor. Especially on the advancing blade side the active rotor shows an additional excitation of higher harmonic blade flap oscillations.

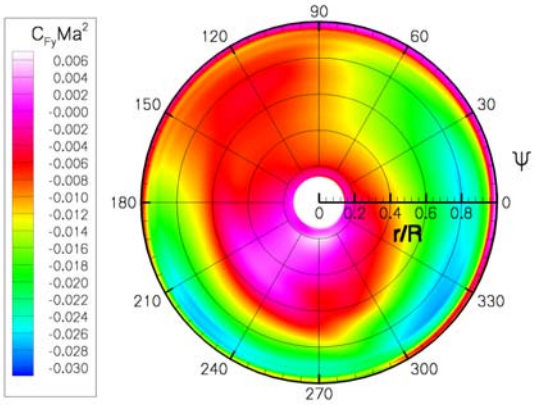

Figure 29: Drag distribution over rotor disk for passive rotor

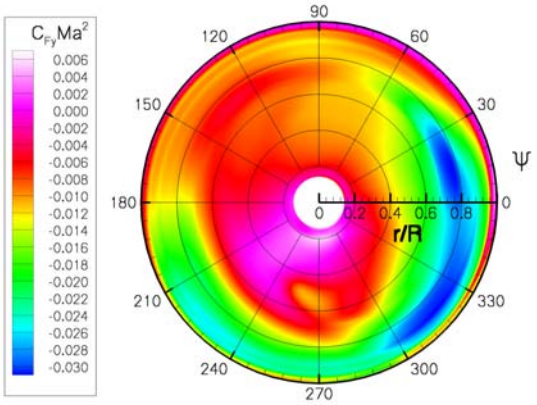

Figure 30: Drag distribution over rotor disk for active rotor

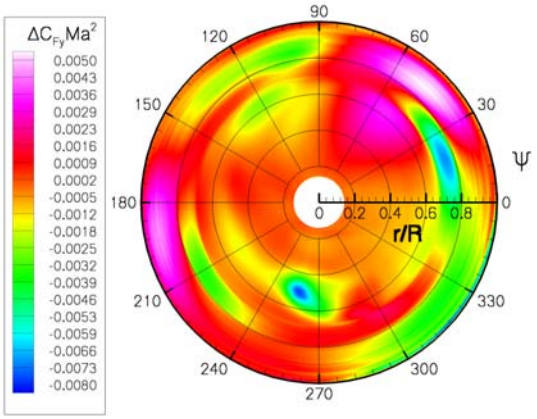

Figure 31: Difference in drag distribution between active and passive rotor

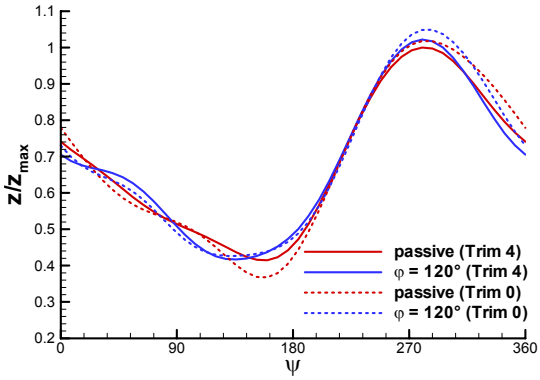

Figure 32: Tip flap deflection comparison between active and passive rotor

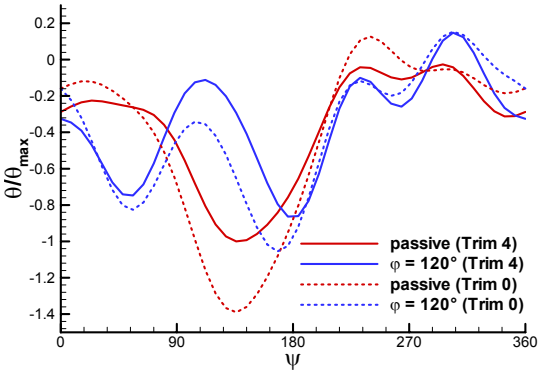

Figure 33: Comparison of elastic tip torsion between active and passive rotor

Larger differences arise in the elastic tip torsion depicted in Figure 33. For both the active and the passive rotor, the initial HOST trim is in good agreement with the final trimmed solution, especially with respect to the phase position. For the active rotor, the influence of the flap input on the tip torsion is clearly visible. As previously stated, the maximum upward flap deflection at $\psi = 120°$ and $\psi = 300°$ are followed by positive peaks in the elastic tip torsion. Whereas the downward flap deflection at $\psi = 30°$ is followed by the local minimum at $\psi = 50°$. The pronounced minimum of the passive rotor at $\psi = 140°$ is shifted to $\psi = 180°$ by the downward deflection, reaching its maximum amplitude at $\psi = 210°$.

Conclusions & Perspectives

A weak coupling method between the Navier-Stokes solver FLOWer[12] and the flight mechanics code HOST[9] was presented. The method was applied to an advanced rotor configuration featuring active trailing edge flaps. The main objective of this paper was the investigation of the power consumption of an active flap rotor. A 2/rev flap control law was applied in conjunction with the standard pitch control. A forward flight case with a moderate advance ratio of $\mu = 0.3$ was selected. The power consumption was compared to a passive rotor, thus controlled by collective and cyclic pitch input only. Both active and passive rotors have been trimmed for the same thrust and longitudinal and lateral mast moment.

For a fixed flap amplitude of 6° the active rotor performance variation has been investigated at six flap phase angles covering one period of the flap movement with a $\Delta\varphi' = 60°$ resolution. An increase in power consumption compared to the passive rotor was observed at all phase angles for the trimmed solution. However, a relative power minimum of the active rotor could be detected for a maximum upward flap deflection at $\psi = 120°$. For this flap phase angle a 2% increase in the power consumption is observed compared to the passive rotor.

It can be stated that the weak coupling strategy is well suited for the performance evaluation of active advanced rotors. Both the passive and the active rotor obtain a trimmed solution within four re-trim cycles. The HOST flap model is able to correctly predict the global influence of the flap control on the rotor trim. However, the CFD solution reveals a complex, highly three-dimensional flow field and thus, significant differences between the 2D HOST loads and the CFD loads are observed for local load distributions. Therefore, the authors are convinced that reliable statements on the performance of active rotors can only be made in an interdisciplinary manner involving flight mechanics and CFD.

Future activities are an investigation of the same flap control law with a reduced flap-amplitude. A power reduction for the present advance ratio could possibly be achieved even with a reduced flap amplitude. Furthermore, a faster forward flight case with an advance ratio greater than $\mu = 0.3$ will be investigated. The increasing influence of transonic and dynamic stall effects might also increase the potential of the active rotor control with respect to a power and thus performance gain.

In addition, it is planned to extend the investigations towards decent flight cases, for which BVI is likely to occur. A 2/rev control law should be able to exert a positive influence on the miss-distance between the blade tip vortex and the rotor blade.

Finally, the method must be validated with respect to flight test data, in order to give final conviction to the present findings.

Acknowledgments

The authors would like to thank the German ministry of Economy and Labour (BMWA) for its funding in the framework of CHANCEII (grant 20H0303A) and LARS (grant 20H0304A).

References

[1] Kloeppel, V., Enenkl, B., and Strehlow, H.: *"Rotor Blade Control by Active Helicopter Servo Flaps"*, International Forum on Aeroelasticity and Structural Dynamics 2005, Munich, Germany, June 2005.

[2] Altmikus, A. Wagner, S., Beaumier, P., Servera, G.: *"A Comparison: Weak versus Strong Modular Coupling for Trimmed Aeroelastic Rotor Simulations",* American Helicopter Society 58th Annual Forum, June 2002.

[3] Servera, G., Beaumier, P., Costes, M.: *"A weak coupling method between the dynamics code HOST and the 3D unsteady Euler code WAVES"*, 26th European Rotorcraft Forum, The Hague (The Netherlands), Sept. 2000.

[4] Shaw, J., Albion, N., Hanger, E.J., Jr., and Teal, R.S.: *"Higher Harmonic Control: Wind Tunnel Demonstration of Fully Effective Vibratory Hub Force Suppression"*, Proceedings, American Helicopter Society 41st Annual Forum, Fort Worth, TX, May 1985.

[5] Jacklin, S.A., Nguyen, K.Q., Blass. A., and Richter, P.: *"Full-Scale Wind Tunnel Test of a Helicopter Individual Blade Control System"*, Proceedings, American Helicopter Society 50th Annual Forum, Washington, DC, May 1994.

[6] Cheng, R., Theodore, C.R., and Celi, R.: *"Effects of Two/rev Higher Harmonic Control on Rotor Performance"*, Journal of the American Helicopter Society, Vol. 48, No. 1, pp. 18-27, January 2003.

[7] Patt, D., Liu, L., and Friedmann, P.: *"Active Flaps for Noise Reduction: A Computational Study"*, American Helicopter Society 61st Annual Forum, Grapevine, TX, June 2005.

[8] Pahlke, K., Van der Wall, B., *"Calculation of Multibladed Rotors in High-Speed Forward Flight with weak Fluid-Structure-Coupling"*, 27th European Rotorcraft Forum, Moscow, Russia, September 2001.

[9] Toulmay, F., Arnaud, G., Falchero, D. and Villat, V.: *"Analytical Prediction of the Rotor Dynamics for Advanced Geometry Blades",* American Helicopter Society, 52nd Annual Forum, Washington, D.C., June 1996.

[10] Enenkl, B., Klöppel, V., Preißler, D., and Jänker, P.: „Full Scale Rotor with Piezoelectric Actuated Blade Flaps", Paper 89, 28th European Rotorcraft Forum, Bristol, UK, September 2002.

[11] Benoit, B., Dequin, A-M., Kampa, K., Grünhagen, W. v., Basset, P-M., Gimonet, B.: *"HOST: A General Helicopter Simulation Tool for Germany and France",* American Helicopter Society, 56th Annual Forum, Virginia Beach, Virginia, May 2000.

[12] Kroll, N., Eisfeld, B. and Bleecke, H.M., "*The Navier-Stokes Code FLOWer",* Volume 71 of Notes on Numerical Fluid Mechanics, pages 58-71. Vieweg, Braunschweig, 1999.

[13] Jameson, A., Schmidt, W. and Turkel, E.: *"Numerical Solutions of the Euler Equations by Finite Volume Methods Using Runge-Kutta Time-Stepping Schemes",* AIAA-Paper 81-1259, 1981.

[14] Jameson, A.: *"Time Dependent Calculation Using Multigrid, With Applications to Unsteady Flows Past Airfoils and Wings",* AIAA-Paper 91-1596, 1991.

[15] Pahlke, K. G.: *"Berechnung von Strömungsfeldern um Hubschrauber-rotoren im Vorwärtsflug durch die Lösung der Euler-Gleichungen",* DLR-Forschungs-bericht 1999-22, ISSN 1434-8454, 1999.

[16] Altmikus, A. R. M. and Wagner, S.: *"CHANCE - Complete Helicopter Advanced Computational Environment: WP 4.2 Full Coupling and Trim"* 2. Advancement Report, Reporting Period: 01.01.2000 - 31.12.2000, Institut für Aero- und Gasdynamik, Universität Stuttgart, 2001.

[17] Jeong, J., Hussain, F., *"On the Identification of a Vortex"*, Journal of Fluid Mechanics, Vol. 285, pp. 69-94, 1995.